A generalized power law approximation for fluvial incision of bedrock channels

Nicole M. Gasparini[1] and Mark T. Brandon[2]

Received 2 January 2010; revised 16 February 2011; accepted 11 March 2011; published 17 June 2011.

[1] Sediment flux is known to influence bedrock incision rates in mountain rivers. Although the widely used stream power incision model lacks any explicit representation of sediment flux, the model appears to work in a variety of real settings. We address this apparent contradiction using numerical experiments to explore the morphology of fluvial landscapes evolved with four different incision models, three of which include the influence of sediment flux on incision rate. The numerical landscapes have different spatial patterns of uplift and are at steady state. We analyze these landscape using the common "stream power" approach, which views incision rates to be primarily a function of the local channel gradient S and the upstream drainage area A. We find that incision rates I for these landscapes are well described by an empirical power law equation $I = K'A^{m'}S^{n'}$. This equation is functionally equivalent to the widely used stream power model, with the important distinction that the parameters K', m', and n' are entirely empirical. These parameters take on constant values within a single landscape, but can otherwise be quite different between landscapes mainly due to differences in the pattern of rock uplift within the drainage. In particular, the parameters m' and n' decrease as the rate of rock uplift becomes more focused in the upland part of a mountain belt. The parameter m' is particularly important in that it describes the sensitivity of a tectonically active mountain belt to changes in precipitation or tectonic accretion. It also defines how incision rates will change as the discharge becomes flashier.

Citation: Gasparini, N. M., and M. T. Brandon (2011), A generalized power law approximation for fluvial incision of bedrock channels, *J. Geophys. Res.*, *116*, F02020, doi:10.1029/2009JF001655.

1. Introduction

[2] An important objective in geomorphology is to understand the relationship between geomorphic processes and the local form of the landscape, as represented by the spatial variation in gradient, curvature, and upslope catchment area [*Dietrich et al.*, 2003]. An example of this kind of approach is the stream power incision model, $I = KA^mS^n$, where incision rate I in a bedrock river is solely a function of S, the local channel gradient, and A, the drainage area above that point [e.g., *Howard*, 1980; *Howard and Kerby*, 1983; *Howard et al.*, 1994; *Rosenbloom and Anderson*, 1994; *Seidl and Dietrich*, 1992; *Tucker and Slingerland*, 1996; *Whipple and Tucker*, 1999]. This model, or derivations of it, have been widely used to study the evolution and shape of bedrock river profiles [e.g., *Duvall et al.*, 2004; *Finnegan et al.*, 2005; *Kirby and Whipple*, 2001; *Ouimet et al.*, 2009; *Roe et al.*, 2002; *Snyder et al.*, 2000; *Stock and Montgomery*, 1999; *Tucker and Whipple*, 2002; *Whipple and Tucker*, 2002; *Whittaker et al.*, 2007; *Wobus et al.*, 2003, 2006; *Yanites et al.*, 2010], and to analyze the interaction of climate and topography in tectonically active mountain ranges [e.g., *Hilley and Strecker*, 2004; *Hilley et al.*, 2004; *Roe et al.*, 2006, 2008; *Stolar et al.*, 2006; *Whipple and Meade*, 2004; *Whipple*, 2009].

[3] The stream power model has been tested with variable success using bedrock rivers with well-defined incision patterns [e.g., *Stock and Montgomery*, 1999; *Tomkin et al.*, 2003; *van der Beek and Bishop*, 2003; *Whittaker et al.*, 2007; *Yanites et al.*, 2010]. The functional form of the model seems to work well, but the estimates for the parameters m and n can differ from commonly expected values [*Stock and Montgomery*, 1999; *Tomkin et al.*, 2003; *van der Beek and Bishop*, 2003]. However, the model is still widely used and our confidence in the model may be based on the fact that many of the fundamental relationships of fluvial hydrology take the form of power law functions [e.g., *Leopold et al.*, 1964].

[4] Despite its widespread use, the stream power model remains incomplete, in that it ignores the influence of sediment flux on incision rates [e.g., *Chatanantavet and Parker*, 2008, 2009; *Cowie et al.*, 2008; *Finnegan et al.*, 2007; *Johnson and Whipple*, 2007; *Johnson et al.*, 2009; *Sklar and Dietrich*, 2001, 2004, 2006; *Turowski et al.*,

[1]Department of Earth and Environmental Sciences, Tulane University, New Orleans, Louisiana, USA.
[2]Department of Geology and Geophysics, Yale University, New Haven, Connecticut, USA.

0148-0227/11/2009JF001655

2007]. When the sediment flux is low, the amount of sediment bed cover is small so moving bed load will impact the bed and serve as tools that enhance incision rates. As the sediment flux increases and sediment begins to cover the channel bed, there is a decrease in the area of bedrock exposed to sediment impacts, resulting in a decrease in incision rate.

[5] In this paper, we focus not on the stream power model, but rather its functional form

$$I \approx K' A^{m'} S^{n'}, \tag{1}$$

where the primes are used to indicate that the parameters K', m', and n' are entirely empirical. The key questions are (1) Does this function provide a useful approximation of the distribution of incision rates at the drainage network scale? and (2) What controls variation of m' and n' values? Our approach is to test the ability of the power law approximation to predict incision rates in numerically generated landscapes evolved using different fluvial incision processes and different patterns of rock uplift. The CHILD landscape evolution model [e.g., *Tucker et al.*, 2001a, 2001b] is used to calculate steady state landscapes and a least squares method is used to estimate m' and n'. These parameters provide information about the sensitivity of incision rate to changes in discharge and channel slope. Thus, the range in m' and n' values has important implications for the feedbacks between climate and mountain building, and also the sensitivity of fluvial incision to extreme discharge events.

[6] Our analysis is divided into four parts. The first section provides a summary of the four incision models used in our different numerical modeling scenarios, which we refer to as numerical experiments. The second section discusses the predicted values for K', m', and n', which are based on a truncated Taylor series approximation for each of the incision models. The third section presents the least squares method used to estimate K', m', and n' from the numerical experiments. The fourth section presents the setup and results of the numerical experiments.

2. Bedrock Incision Models

[7] We consider four models for bedrock incision in this study. The models are distinguished in the way that they account for sediment flux. The first model we describe is the stream power model (section 2.1), which does not include a sediment flux term in the incision equation. The next two models are the saltation-abrasion (section 2.2) and generalized abrasion (section 2.3) models, which are based on the work of *Sklar and Dietrich* [2004] and *Parker* [2004], respectively. Both of these models include the influence of sediment flux on bedrock incision. The last model is the transport-limited model, in which the divergence of sediment flux controls bedrock incision. The four incision models considered here are described in detail by *Crosby et al.* [2007] and *Gasparini et al.* [2007] and are formulated assuming a steady flow with a single grain size.

[8] The stream power, saltation-abrasion and generalized abrasion models are detachment limited, meaning that the rate controlling process is the removal of material from a bedrock channel. These models have the general form

$$I \propto f(Q_s)\tau_b^{p_1}, \tag{2}$$

where τ_b is the basal shear stress, p_1 is a scaling exponent, and $f(Q_s)$ is the sediment-flux erodibility function, which accounts for the influence of sediment flux on bedrock incision. The stream power model does not include sediment flux ($f(Q_s) = 1$), and thus could be viewed as an approximation for a river with little to no bed load. Both the saltation-abrasion and generalized abrasion models account for the dual role of sediment as both tools and cover, and thus apply in rivers with varying bed load transport conditions. The only difference between these two models is that the generalized abrasion model does not account for variable hop length of saltating bed load, which is included in the saltation-abrasion model.

[9] The fourth incision model is the transport-limited model, in which erosion rates are limited by the rate at which bed load can be transported through the channel. This model represents the end-member case in which material is easily detached from the channel bed, and the sediment flux is everywhere at the maximum capacity. It can be applied to bedrock channels that are entirely covered in sediment or channels in which the bedrock is relatively weak and easily detached from the bed. The incision rate is determined entirely by conservation of mass,

$$I = \frac{1}{W}\frac{\mathrm{d}Q_t}{\mathrm{d}s}, \tag{3}$$

where W is the channel width, Q_t is the volumetric sediment transport rate, and s is the channel length.

[10] These models have many similar components, so we start here with a description of those relationships that are common to the models. The first variable is water discharge Q_w, which is related to channel width W and drainage area A by the following relationships [e.g., *Wolman and Miller*, 1960]

$$Q_w \sim A^c, \tag{4a}$$

$$W \sim A^{bc}, \tag{4b}$$

and

$$\frac{Q_w}{W} \sim A^{c(1-b)}. \tag{4c}$$

We use the ~ symbol to indicate that the quantity of the left side of the expression scales with the quantity on the right side of the expression. The ~ symbol implies that this is an approximation and a proportional relationship. Commonly used values for the scaling exponents are $b = 1/2$ and $c = 1$ [see *Whipple and Tucker*, 1999]. These equations implicitly account for the relationship between precipitation and discharge.

[11] The next variable is basal shear stress τ_b, which represents the shear stress generated by water moving across the channel bed. For uniform, steady flow in a wide channel

$$\tau_b \sim \left(\frac{Q_w}{W}\right)^{p_2} S^{p_3} = A^{c(1-b)p_2} S^{p_3}, \tag{5}$$

Table 1. Summary of Numerical Experiments

Experiment	K[a]	m_i	n_i	K_t[a]	m_t	n_t	Uplift[b]
Saltation-Abrasion, Nonlinear							
sa_pup_1	6.00E-02	−0.25	−0.5	5.00E-06	1.5	1	fast
sa_pup_2	4.00E-02	−0.25	−0.5	1.00E-05	1.5	1	fast
sa_pup_3	4.00E-02	−0.25	−0.5	1.00E-05	1.5	1	slow
Generalized Abrasion, Nonlinear							
ga_pup_1	2.00E-03	0	0	6.00E-06	1.5	1	fast
ga_pup_2	2.00E-03	0	0	1.00E-05	1.5	1	fast
ga_pup_3	2.00E-03	0	0	1.00E-05	1.5	1	slow
Transport-Limited, Nonlinear							
tl_pup_1	–	–	–	4.00E-06	1.5	1	fast
Stream Power, Nonlinear							
sp_pup_1	1.00E-05	0.5	1	–	–	–	fast
sp_pup_2	1.00E-05	0.5	1	–	–	–	slow
sp_pup_3	3.00E-06	0.5	1	–	–	–	fast
sp_pup_4	5.00E-06	0.5	1	–	–	–	slow
sp_pup_5	5.00E-06	0.5	1	–	–	–	fast
Saltation-Abrasion, Linear							
sa_lup_1	6.00E-02	−0.25	−0.5	5.00E-06	1.5	1	slow
sa_lup_2	4.00E-02	−0.25	−0.5	1.00E-05	1.5	1	fast
sa_lup_3	4.00E-02	−0.25	−0.5	1.00E-05	1.5	1	slow
Generalized Abrasion, Linear							
ga_lup_1	2.00E-03	0	0	6.00E-06	1.5	1	slow
ga_lup_2	2.00E-03	0	0	1.00E-05	1.5	1	fast
ga_lup_3	2.00E-03	0	0	1.00E-05	1.5	1	slow
Transport-Limited, Linear							
tl_lup_1	–	–	–	6.00E-06	1.5	1	slow
tl_lup_2	–	–	–	4.00E-06	1.5	1	slow
Stream Power, Linear							
sp_lup_1	1.00E-05	0.5	1	–	–	–	slow
sp_lup_2	1.00E-05	0.5	1	–	–	–	fast
sp_lup_3	5.00E-06	0.5	1	–	–	–	slow
sp_lup_4	3.00E-06	0.5	1	–	–	–	slow

[a]Units for these variables are consistent with distance in meters, area in square meters, slope as a gradient (dimensionless), and incision rate in meters per year. K refers to the proportionality constant for the relevant incision model for each experiment.
[b]Uplift type defined in Table 2.

where p_2 and p_3 are scaling exponents that are both equal to 2/3 when the Darcy-Weisbach flow-resistance equation is used [e.g., *Tucker and Slingerland*, 1996].

[12] The maximum capacity for sediment transport is often described by [e.g., *Meyer-Peter and Müller*, 1948; *Sinha and Parker*, 1996]

$$Q_t \sim W(\tau_b - \tau_c)^{3/2}, \tag{6}$$

where τ_c is the threshold shear stress for entrainment of sediment. *Sinha and Parker* [1996] show that the threshold effect can be replaced by a power law approximation

$$Q_t \sim W\tau_b^{p_4}, \tag{7}$$

where $p_4 = \frac{3}{2}\left(\frac{\tau_{b0}}{\tau_{b0}-\tau_c}\right)$ and τ_{b0} is the bed shear stress at the center of the interval for this approximation. This approximation indicates that $p_4 > 3/2$ when $\tau_{b0} > \tau_c$. Our numerical experiments are focused exclusively on transport of a single-grain size in a steady flow where $\tau_b > \tau_c$, so it is reasonable to replace (6) with (7). Equations (4), (5), and (7) indicate that transport capacity can be approximated by [*Howard*, 1980]

$$Q_t \approx K_t A^{m_t} S^{n_t}, \tag{8}$$

where K_t is a dimensional constant, and m_t and n_t are scaling exponents. The relationships above suggest that $m_t \geq 1$, and $n_t \geq 1$. We increase the value of m_t to 3/2 in order to generate landscapes with realistic concavity values (see, e.g., *Tucker and Bras* [1998], *Whipple and Tucker* [2002], and *Willgoose et al.* [1991] for details). All parameter values are given in Table 1.

[13] We now focus on the three detachment-limited models. Combining equations (2) and (5) gives a generalized equation for detachment-limited incision

$$I \approx K f(Q_s) A^{m_i} S^{n_i}, \tag{9}$$

where K is a dimensional constant related to bedrock erodibility and precipitation, and m_i and n_i are scaling exponents, which depend on the value of p_1 in equation (2). The subscript i is used to indicate that these exponents take on different values for each incision model.

2.1. Stream Power Model

[14] Setting $f(Q_s)$ to a constant in equation (8) results in the stream power model, which has been widely used in landscape evolution models [e.g., *Anders et al.*, 2008; *Howard*, 1994; *Miller and Slingerland*, 2006; *Pelletier*, 2010; *Roe et al.*, 2003; *Stock and Montgomery*, 1999; *Stolar et al.*, 2006; *Whipple and Tucker*, 1999]:

$$I \approx K_{SP} A^{m_i} S^{n_i}. \tag{10}$$

One can derive values for m_i and n_i depending on whether the stream power model is based on unit stream power or shear stress. The values of m_i, and perhaps n_i as well, are likely influenced by other factors, including downstream changes in channel width and discharge [e.g., *Finnegan et al.*, 2005; *Whittaker et al.*, 2007; *Yanites et al.*, 2010]. In this study, we set $m_i = 1/2$ and $n_i = 1$, which is equivalent to setting $p_1 = 3/2$ in (2). K_{SP} is a coefficient that varies as a function of climate and rock resistance to incision.

[15] The stream power model is unique when compared with the other incision models used here because the incision rate is solely a function of A and S. As a result, the steady state morphology of a landscape with any rock uplift pattern or precipitation distribution is easily predicted. The simplicity of the stream power model makes it useful as a reference case for the other models.

2.2. Saltation-Abrasion Model

[16] The saltation-abrasion model used here is described by *Crosby et al.* [2007] and *Gasparini et al.* [2007], and follows, with some simplifications, from *Sklar and Dietrich* [2004]. The sediment-flux erodibility function is

$$f(Q_s) \approx \frac{Q_s}{W}\left(1 - \frac{Q_s}{Q_t}\right), \tag{11}$$

where Q_s is the incoming volumetric sediment flux, and Q_t is the volumetric sediment transport capacity (8). Equation (11) can be recast as

$$f(Q_s) = \frac{Q_t}{W}\mathcal{R}(1-\mathcal{R}), \tag{12}$$

where $\mathcal{R}$, the flux-capacity ratio, is equal to $\frac{Q_s}{Q_t}$ and can be viewed as a measure of the amount of bedcover. $\mathcal{R}$ ranges from 0 for a river with no bed load to 1 for a river at full capacity. The saltation-abrasion model has the form

$$I \sim \frac{Q_t}{W}\mathcal{R}(1-\mathcal{R})\tau_b^{-3/4}. \tag{13}$$

The negative exponent on shear stress comes from the dynamics of a saltating bed load moving over a planar bed [*Sklar and Dietrich*, 2004]. As the sediment hop length increases, individual grains impact the bed less frequently, and do less work on the bed. Substituting (5) for shear stress gives

$$I \approx K_{SA}\frac{Q_t}{W}\mathcal{R}(1-\mathcal{R})A^{m_i}S^{n_i}, \tag{14}$$

where $m_i = -1/4$ and $n_i = -1/2$. K_{SA} is a dimensional constant that varies as a function of climate and rock resistance to erosion (see *Gasparini et al.* [2007] for details).

2.3. Generalized Abrasion Model

[17] The generalized-abrasion model is simplified after *Parker* [2004] and uses the same function for $f(Q_s)$ as (11) [*Gasparini et al.*, 2007]. This model does not include saltation dynamics, and as a result there is no shear-stress dependence, implying that $p_1 = 0$ in (2). The resulting equation is

$$I \approx K_{GA}\frac{Q_t}{W}\mathcal{R}(1-\mathcal{R}), \tag{15}$$

where K_{GA} is a coefficient that varies as a function of rock resistance to erosion.

2.4. Transport-Limited Model

[18] The transport-limited case is defined by the change in sediment load along a reach,

$$I = \frac{1}{W}\frac{\mathrm{d}Q_t}{\mathrm{d}s} = \frac{1}{W}\frac{\mathrm{d}Q_s}{\mathrm{d}s}. \tag{16}$$

Equation (16) is simply equation (3) recast to show the flux of moving bed load, Q_s, is always equal to the local transport capacity, Q_t, as defined by (8) with $m_t = 3/2$ and $n_t = 1$. The incision rate that occurs over a channel interval, Δs, is always proportional to the change in transport capacity, ΔQ_t, over that interval. It is often assumed that at steady state Q_s can be set to the product of the upstream area and the rock uplift rate. This assumption only holds when the rock uplift rate is uniform upstream and the entire upstream channel network is at steady state. The CHILD model routes sediment, so it can accurately account for temporal and spatial variations in sediment flux, and the influence of this variation on local incision rates [*Tucker et al.*, 2001a]. We do not include a porosity term in equation (15) [e.g., *Willgoose et al.*, 1991] because porosity would only affect the trend in the results if porosity varied systematically in space. In our numerical experiments, both grain size and porosity are uniform.

3. Prediction of Power Law Parameters

[19] The evolution of any system can be reduced to a problem of integration, where relevant processes within the system are represented by a system of differential equations. The domain of the integration is usually finite, so the conditions along the boundary of the system must be specified, both in space and in time. Landscape evolution models provide the numerical machinery to solve this integration. The governing differential equations in a landscape evolution model must provide an internally consistent description of the processes associated with production and transport of water and sediment.

[20] We would like to examine, test, and compare different incision models under different boundary conditions, however the space of realizable landscapes is beyond what we can reasonably explore with numerical experiments. We use scaling analysis to understand the general behavior of the incision models [*Meakin*, 1998]. The first step is to reduce the number of independent variables to the smallest number needed to represent the state of the system. For our analysis here, we follow the conventional wisdom that the variation in incision rate at a point is primarily a function of only two independent variables, A and S. The second step is to simplify the incision equations into a common linearized form. Each of the equations is a nonlinear function composed of different combinations of power functions. In scaling analysis, the usual approach is to replace a nonlinear equation with a Taylor-series approximation (see *Hassani* [2009] for a good review of Taylor series). The analysis is simplified by transforming the equation into log space and then applying the Taylor-series expansion [*Savageau and Voit*, 1987; *Savageau*, 1988; *Voit*, 2000].

[21] To illustrate the power law approximation, we use a generic incision equation $I = I(A, S)$, which is solely a function of area and slope. More complex functions could be considered, but this is beyond the scope of our study here. The first step is to recast the incision equation with logarithmic variables $\iota = \iota(\alpha, \sigma)$, where $\iota = \ln I$, $\alpha = \ln A$, and $\sigma = \ln S$. Next, we define the center point for the interval of approximation, which is given by the coordinates ι_0, α_0, σ_0. The Taylor-series expansion is

$$\iota(\alpha,\sigma) = \iota_0 + (\alpha-\alpha_0)\left(\frac{\partial \iota}{\partial \alpha}\right)_0 + (\sigma-\sigma_0)\left(\frac{\partial \iota}{\partial \sigma}\right)_0 + R_N(\alpha,\sigma), \tag{17}$$

where R_N refers to the higher-order terms of the series, which are ignored for the approximation. The subscript 0 outside the partial derivatives indicates that they are evaluated at the center point, α_0, σ_0. When this approximation is returned back to the original form with linear and not log variables, the power law form is apparent, $I \approx K' A^{m'} S^{n'}$ (equation (1)), where the constant $K' = \exp\left[\iota_0 - \alpha_0\left(\frac{\partial \iota}{\partial \alpha}\right)_0 - \sigma_0\left(\frac{\partial \iota}{\partial \sigma}\right)_0\right]$. The exponents are given by

$$m' = \left(\frac{\partial \iota}{\partial \alpha}\right)_0 = \left(\frac{\partial \ln I}{\partial \ln A}\right)_0 = \left(\frac{A}{I}\frac{\partial I}{\partial A}\right)_0, \tag{18a}$$

and

$$n' = \left(\frac{\partial \iota}{\partial \sigma}\right)_0 = \left(\frac{\partial \ln I}{\partial \ln S}\right)_0 = \left(\frac{S}{I}\frac{\partial I}{\partial S}\right)_0. \tag{18b}$$

These equations show two important features about the power law representation. The first is that partial derivatives can be determined directly from the incision equation. The second is that the exponents represent dimensionless scaling factors that indicate how the incision rate is influenced by changes in area or slope. In other words, $\frac{\Delta I}{I} \approx m' \frac{\Delta A}{A}$, and $\frac{\Delta I}{I} \approx n' \frac{\Delta S}{S}$, as long as the ratios remain small (i.e., less than about 50 percent). For example, a m' value of 0.5 would mean that a 10 percent change in drainage area would cause a 5 percent change in incision rate, assuming that all other factors remain constant.

[22] The Taylor-series expansion requires that the log-transformed incision function is infinitely differentiable at α_0, σ_0, which is true for all of the incision models considered here. The error associated with the approximation generally increases with increasing distance from the center point. The convergence properties of the series can be used to determine an upper bound for the error but this is a complicated task for a multivariate Taylor series. Each term in the remainder of the series R_N consists of a successively higher-order derivative multiplied by a difference, either $(\alpha - \alpha_0)$ or $(\sigma - \sigma_0)$, raised to a successively higher integer power. We can infer that the R_N will remain convergent (and thus relatively small compared to the leading terms) while in the interval defined by $|\alpha - \alpha_0| < 1$ and $|\sigma - \sigma_0| < 1$. In other words, we should be able to trust the approximation out to at least one log unit from the center point, which is equivalent to $\sim 0.37 < (A/A_0) < \sim 2.72$ and $\sim 0.37 < (S/S_0) < \sim 2.72$ (the numbers correspond to e^{-1} and e). *Voit and Savageau* [1987] show that the power law representation commonly remains valid over a much larger range for biochemical reactions, sometimes up to two or three orders of magnitude. The numerical experiments presented below help to illustrate the useful range for the power law approximation when applied to the problem of fluvial incision.

[23] We now apply this power law approximation to the incision models in order to obtain predictions for m' and n', which will then be compared against those estimated from the numerical experiments. The prediction is trivial for the stream power model in that m' and n' are equal to the process-based estimates for m_i and n_i, respectively. The two abrasion models are considered first, since they have similar equations. The transport model is considered next.

3.1. Abrasion Models

[24] The two abrasion models are subsumed by the following generalized equation

$$I \sim \mathcal{R}(1-\mathcal{R}) A^{m_i + m_t - bc} S^{n_i + n_t}. \tag{19}$$

The saltation-abrasion model has $m_i = -1/4$ and $n_i = -1/2$, and the general-abrasion model has $m_i = n_i = 0$. Because $\mathcal{R} = \mathcal{R}(Q_t, Q_s)$, we need to find a representation for Q_s before we can calculate the approximation. We assume that Q_s is closely approximated by a power law equation

$$Q_s \approx K_s' A^{m_s'} S^{n_s'}, \tag{20}$$

where K'_s, m'_s, and n'_s are empirical parameters. For steady state landscapes, Q_s is commonly assumed to be solely a function of area, but this is only true for a spatially uniform uplift rate. If uplift and incision rates are not spatially uniform, area alone cannot constrain sediment flux values. This is illustrated in our numerical modeling results.

[25] The partial derivatives of (19) give the following predicted values for the power law exponents:

$$\begin{aligned}\langle m' \rangle &= \left(\frac{A}{I}\frac{\partial I}{\partial A}\right)_0 = (m_i + m_t - bc) \\ &\quad + \left(\frac{A}{\mathcal{R}(1-\mathcal{R})}\frac{\partial[\mathcal{R}(1-\mathcal{R})]}{\partial \mathcal{R}}\frac{\partial \mathcal{R}}{\partial A}\right)_0 \\ &\approx \ldots (m_i + m_t - bc) + (m_s' - m_t)\frac{1 - 2\mathcal{R}_0}{1 - \mathcal{R}_0},\end{aligned} \tag{21a}$$

and

$$\begin{aligned}\langle n' \rangle &= \left(\frac{S}{I}\frac{\partial I}{\partial S}\right)_0 = (n_i + n_t) \\ &\quad + \left(\frac{S}{\mathcal{R}(1-\mathcal{R})}\frac{\partial[\mathcal{R}(1-\mathcal{R})]}{\partial \mathcal{R}}\frac{\partial \mathcal{R}}{\partial S}\right)_0 \\ &\approx \ldots (n_i + n_t) + (n_s' - n_t)\frac{1 - 2\mathcal{R}_0}{1 - \mathcal{R}_0},\end{aligned} \tag{21b}$$

where $\mathcal{R}_0$ is the sediment-flux capacity at the center of the approximation interval. The brackets $\langle \cdot \rangle$ are used to indicate that these estimates are the "expected values" for m' and n', as derived directly from the incision models. The "approximately equal" symbol is used to remind us that that the predictions on the right sides of (21a) and (21b) include an approximate relationship for sediment flux (20).

3.2. Transport-Limited Incision

[26] We start by recasting the transport-limited model (16) in terms of A and S. Hack's law [*Hack*, 1957], $s \sim A^h$, provides the scaling relationship between channel distance s and area. Hack's constant h is ~0.6 for most drainages [*Willemin*, 2000]. In our numerical experiments, h is a little larger, with an average of 0.66, and a range of 0.64 to 0.69. For our purposes, $\frac{1}{W}\frac{\mathrm{d}s}{} \sim \frac{A^{1-h-bc}}{\mathrm{d}A}$, which can be substituted into (16) to give

$$I = \frac{1}{W}\frac{\mathrm{d}Q_t}{\mathrm{d}s} \sim \frac{\mathrm{d}Q_t}{\mathrm{d}A} A^{1-h-bc}. \tag{22}$$

The derivative is given by

$$\frac{\mathrm{d}Q_t}{\mathrm{d}A} \sim A^{m_t - 1} S^{n_t}\left[m_t + n_t \frac{A}{S}\frac{\partial S}{\partial A}\right]. \tag{23}$$

The partial derivative $\frac{\partial S}{\partial A}$ is related to θ, the concavity index of the channel [e.g., *Tucker and Whipple*, 2002]

$$\theta = -\frac{\partial \ln S}{\partial \ln A} = -\frac{A}{S}\frac{\partial S}{\partial A}. \tag{24}$$

The concavity index is the negative of the slope of the log slope–log area trend for an individual channel (e.g., Figure 1). We assume here that θ is approximately constant, but for our numerical experiments this is not entirely the case. This assumption implies that θ has no influence on the exponents

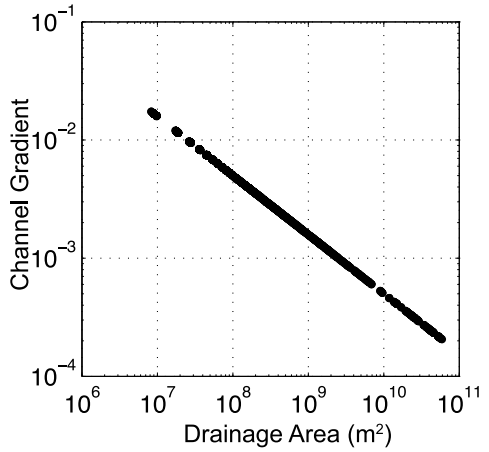

Figure 1. Example of steady state slope area data from a numerical experiment with uniform uplift. These data were produced using the stream power model.

for the power law approximation. The resulting approximation is $I \sim A^{m_t-h-bc}S^{n_t}$, which means that

$$\langle m' \rangle \approx m_t - h - bc \tag{25a}$$

$$\langle n' \rangle \approx n_t. \tag{25b}$$

Once again, the predictions for the exponents are shown as approximations, given that they rely on an empirical relationships and assumptions, such as Hack's law and constant concavity.

4. Estimating Exponents From Results of Numerical Experiments

[27] We use numerical experiments to test whether the power law approximation is valid at the scale of a full drainage. The least squares method provides a straightforward way to test this approximation. In log form, the power law approximation is given by

$$\iota = \ln K' + m'\alpha + n'\sigma + \varepsilon, \tag{26}$$

where ε represents the error in the approximation. This equation represents a plane in ι–α–σ space. It is linear with respect to its parameters $\ln K'$, m', and n', which means that the parameters can be uniquely estimated from a set of three or more independent observations of incision rates in ι–α–σ space.

[28] The log incision–rate variable ι is designated as the dependent variable, which means that the best fit solution will be determined by minimizing the sum of the squares of the residuals $SSR = \sum_{i=1}^{n} (\iota_i^{\text{obs}} - \iota_i^{\text{pred}})^2$, where ι_i^{obs} are the observed incision rates calculated in a numerical experiment, and ι_i^{pred} are the values predicted by the power law equation. The quality of the best fit solution is reported using the usual metric $R^2_{fit} = 1 - \frac{SSR}{SST}$, where $\text{SST} = \sum_{i=1}^{n} [\iota_i^{\text{obs}} - \text{mean}(\iota_i^{\text{obs}})]^2$.

[29] By designating ι as the dependent variable, we are assuming that any misfit is due to errors in that variable. The misfit between observed and predicted incision rates is due to the Taylor-series approximation (17), which ignores the higher-order terms represented by R_N. The misfit appears as an additive term on the right side of the power law approximation (17), so ι is correctly designated as the dependent variable for the numerical experiments considered here. The application of the least squares method is more complicated for real data sets given that all of the variables will have errors, as discussed by *Tomkin et al.* [2003].

[30] Parameter estimation requires that the span of the data is large compared with the errors. In other words, a set of observations must have a large enough distribution of ι–α–σ values to fully resolve the planar geometry of the power law equation. If this is not the case, then there is no unique solution to the inverse problem. This problem occurs when there is a high covariance between the independent variables, which in our case are α and σ. When this happens, the data will tend toward a linear distribution of points (collinearity) in ι–α–σ space, and the least squares model will fail to resolve the planar geometry of the incision equation (26).

[31] As an example, consider a steady state landscape forced by a uniform and steady rate of uplift. The incision rate is everywhere the same, so changes in drainage area are directly compensated by changes in channel slope, which would appear as a linear covariance between α and σ (Figure 1). We can see this result by setting (17) to a fixed incision rate, where $\iota = \iota_0$ (and ignoring R_N as well). The remaining two variables are forced to follow a line in ι–α–σ space, defined by $\iota = \iota_0$ and $\frac{\sigma - \sigma_0}{\alpha - \alpha_0} = \frac{m'}{n'}$. It is impossible to get three or more independent observations from a set of observations that follow a line. As a result the data are insufficient to determine a solution using the least squares method.

[32] To ensure that the model data are able to adequately resolve the power law parameters, we define the numerical experiments to have relatively large spatial variation in uplift rates, and we include incision rates from both tributary and trunk streams. Collinear data sets may be hard to avoid in field studies. In particular, we have found that it is useful to have incision-rate data from both tributaries and trunk channels in order to minimize covariance between slope and area in the data. This holds for both model data and field data (results not shown here). The slope-area plot, which is usually constructed using log-log scaling, can also be inspected to see if the independent variables are collinear (as in Figure 1).

[33] The condition index (CI) method of *Belsley et al.* [1980] and *Belsley* [1991] provides a direct test for the collinearity problem. CI is equal to the square root of the ratio of the largest and smallest eigenvalues of the correlation matrix for the independent variables of the regression (which are α and σ, here). Collinearity may be a problem when CI > 15, and is highly likely when CI > 30. Our practice here is to exclude those numerical experiments that have CI > 15.

5. Numerical Experiments

5.1. Setup of Numerical Experiments

[34] The CHILD model is used to evolve steady state landscapes with different uplift patterns. At steady state, the

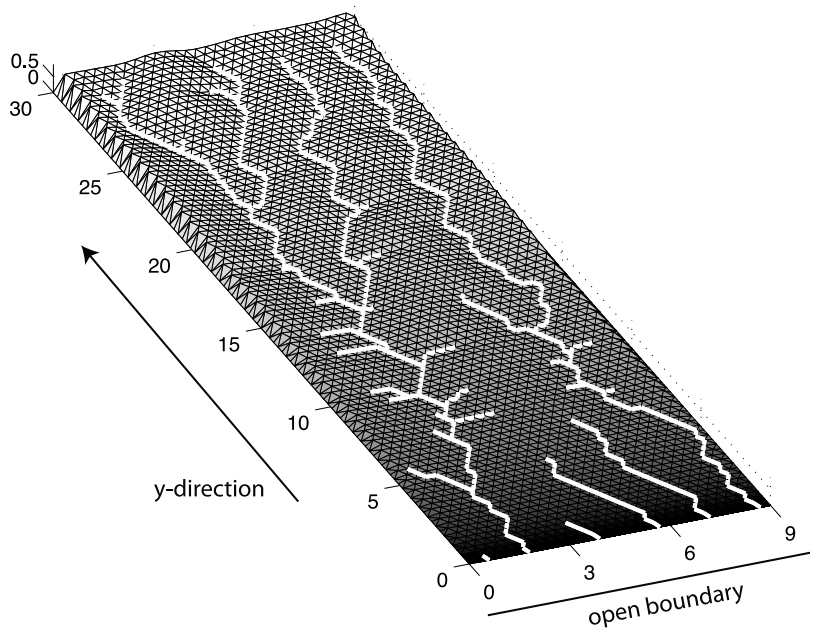

Figure 2. Example of topography created with CHILD (from experiment sa_lup_3). The shading illustrates the uplift pattern, with lowest uplift rates at the open boundary. The values on the axes are in kilometers. The white streamlines illustrate those parts of the network used in the analysis.

incision rate equals the local uplift rate at every location in the landscape. Our methods could be extended to consider transient cases, but we focus here on steady state examples, given that they are simpler and provide an essential first step in understanding the dynamic behavior of the fluvial system.

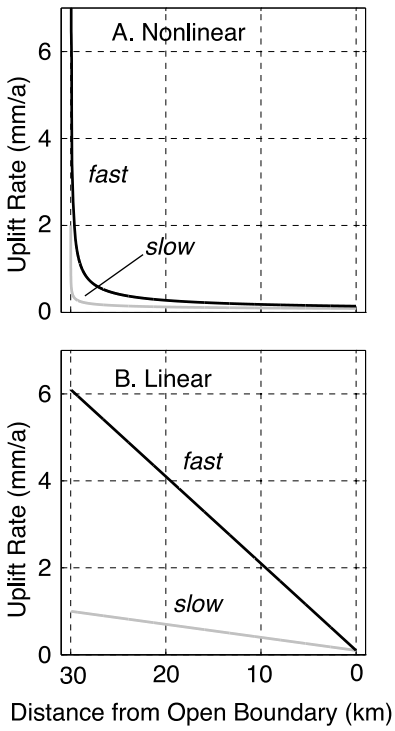

Figure 3. Plots of uplift rate profiles used for our experiments. See Table 2 for details.

[35] All of the numerical landscapes are rectangular in shape, 29.7 km by 8.7 km, with a grid spacing of 300 m. Numerical experiments with a higher resolution, or involving larger or smaller regions (not reported here) indicate that these factors do not significantly influence our estimates of m' and n'. One of the shorter edges of the landscape is an open boundary over which sediment and water can pass out of the system. Material cannot cross the other three edges (Figure 2). The precipitation is uniform and steady, and the discharge is also everywhere steady. The sediment in the drainage network is homogeneous. The initial condition for the landscapes is a white-noise surface with an average elevation of 20 m, and the drainage network evolves on its own. This surface is uplifted and eroded until it reaches steady state.

[36] We used four uplift patterns for our numerical experiments (Table 2 and Figure 3). For all types, uplift varies only in the y direction, with largest values of ≈1.0 to 2.0 mm/a near the drainage divide, to the smallest values of ≈0.1 mm/a close to the open boundary. Uplift is strongly focused at the divide for the two nonlinear uplift patterns, and falls off more gradually with distance for the linear uplift patterns.

Table 2. Parameters for Different Uplift Distribution Used in Experiments

Type of Uplift	Uplift Equation[a]
Type 1: nonlinear and slow	$U = 2(Y_{divide} - y)^{-0.3}$
Type 2: nonlinear and fast	$U = 70(Y_{divide} - y)^{-0.6}$
Type 3: linear and slow	$U = 1 - 0.3 \times 10^{-4}\ (Y_{divide} - y)$
Type 4: linear and fast	$U = 6.1 - 2 \times 10^{-4}\ (Y_{divide} - y)$

[a]Distance y is in meters and uplift rate U is in millimeters per year. Y_{divide} equals 30,000 m.

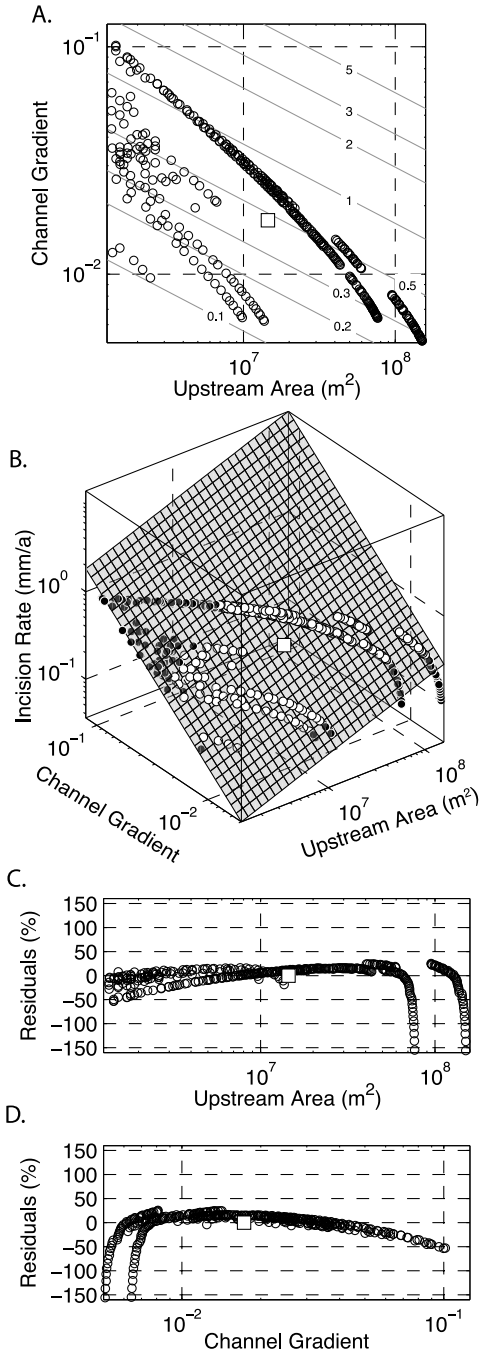

Figure 4. Incision, channel slope, and drainage area data from the landscape and channel network illustrated in Figure 2 (experiment sa_lup_3). (a) The slope area data with iso-incision contours from the best fit power law relationship, labeled in units of millimeters per year. (b) The same data in three dimensions. The gray panel is the best fit power law solution, which is a plane in log I, log S, log A space. White circles are above the plane and black circles are below the plane. (c and d) The residuals in percentage form as a function of drainage area and channel gradient, respectively. Positive values indicate that the observed value is greater than the predicted value, and negative values indicate that the observed value is less than the predicted value. In all of the plots the white square illustrates the centroid of the data, as determined by the log mean.

5.2. Results of Numerical Experiments

[37] Table 3 reports the best fit values of K', m', and n' for each numerical experiment. The R^2_{fit} values range from 0.76–0.99. We focus our presentation on the results from numerical experiment sa_lup_3 (saltation-abrasion model, slow linear uplift; Figures 4 and 5) and sa_pup_3 (saltation-abrasion model, slow nonlinear uplift; Figures 6 and 7). The steady state landscape for the linear uplift example is shown in Figure 2; the slope, area and incision model data and best fit solution are shown in Figure 4 and the slope, area and sediment flux model data and best fit solution are shown in Figure 5. Figures 6 and 7 are similar to Figures 4 and 5, respectively, except that Figures 6 and 7 illustrate the model data and the best fit solutions for the nonlinear example, sa_pup_3. The centroid of the data (Figures 4, 5, 6, and 7) is estimated using the log mean of the data, in keeping with the log scaling associated with the power law approximation.

[38] Figure 4b shows a representation of the three-dimensional best fit plane in log S–log A–log I space and the model data from the linear uplift example that were used to produce this fit. Figures 4c and 4d show the residuals as a function of area and channel slope (note the residuals are shown here as a percent ratio $(I_i^{obs} - I_i^{pred})/I_i^{obs}$ rather than log units). The residuals are below 50% and above −50% over a range of approximately an order of magnitude around the centroid for both area and channel slope.

[39] The slope area plot (Figure 4a) shows contours of incision rate. These contours represent the projection of the best fit plane, shown in Figure 4b, downward onto the log S—log A plane represented by the slope-area plot. The contours have a uniform slope equal to $\frac{m'}{n'}$, which is a conclusion anticipated by the earlier discussion on collinearity. In the case of uniform incision rates, the model data would follow the line representing the contour for that incision rate (e.g., Figure 1). The stream concavity would be equal to $\frac{m'}{n'}$. All of our numerical experiments have spatially variable incision rates, so the trend of the model data is always oblique to the incision-rate contours. Uplift/incision rates for all of our numerical experiments decrease downstream, which means that the channel concavity will always be greater than $\frac{m'}{n'}$ [*Kirby and Whipple*, 2001].

[40] The large span of points in the slope area plot (Figure 4a) is a result of using model data from both the trunk and tributary channels. The map of the drainage (Figure 2) shows several tributaries at about ~5–15 km in the y direction. Each of these tributaries has different incision rates, but they all have small drainage areas relative to the trunk channel. Using model data from both trunk and tributaries, as well as from the small channels that drain directly to the open boundary, increases the spread of the data in area and slope space, and thus should help avoid problems with collinearity.

[41] There is less mismatch between the model incision data and the predicted values in the nonlinear case illustrated in Figure 6 (R^2_{fit} = 0.99) in comparison with the linear case illustrated in Figure 4 (R^2_{fit} = 0.87). As a result, the residuals for the nonlinear example (Figures 6c and 6d) are smaller than the residuals in the linear example (Figures 4c and 4d). In all cases, the numerical experiments using the nonlinear uplift model are better described by the power law approximation (higher R^2_{fit} values and less mismatch) than

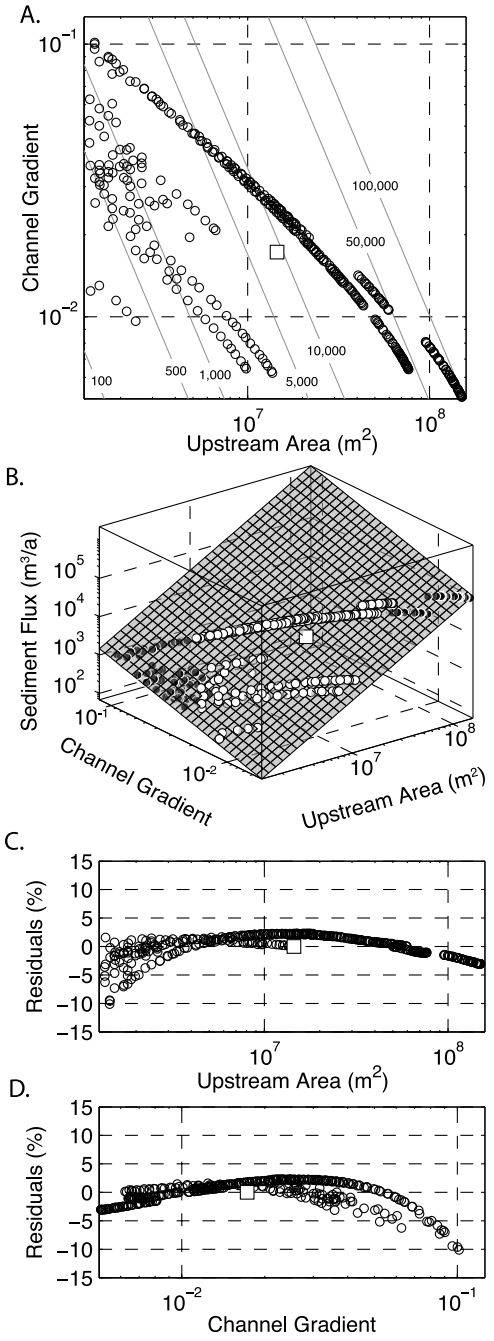

Figure 5. Sediment flux, channel slope, and drainage area data from the landscape and channel network illustrated in Figure 2 (experiment sa_lup_3). (a) The slope-area data with iso-sediment-flux contours from the best fit power law relationship, labeled in units of cubic meters per year. (b) The same data in three dimensions. The gray panel is the best fit power law solution, which is a plane in log Q_s, log S, log A space. White circles are above the plane and black circles are below the plane. (c and d) The residuals in percentage form as a function of drainage area and channel gradient, respectively. Positive values indicate that the observed value is greater than the predicted value, and negative values indicate that the observed value is less than the predicted value. In all of the plots the white square illustrates the centroid of the data, as determined by the log mean.

the numerical experiments using the linear uplift model (Table 3).

[42] Table 4 reports the least squares estimates for power law fits for sediment flux Q_s (equation (20)). In all cases $R^2_{fit} > 0.99$. Figures 5 and 7 illustrate Q_s data taken from the linear and nonlinear uplift examples, respectively. We do not fully understand this result, but it is clearly a robust feature for all numerical experiments. One possibility is that this result is related to the specific form of the uplift equation, but the linear uplift case is actually poorly represented by a power law approximation. Instead, we think that this result is an intrinsic feature associated with fluvial incision. The drainages tend to organize in a way that the sediment flux

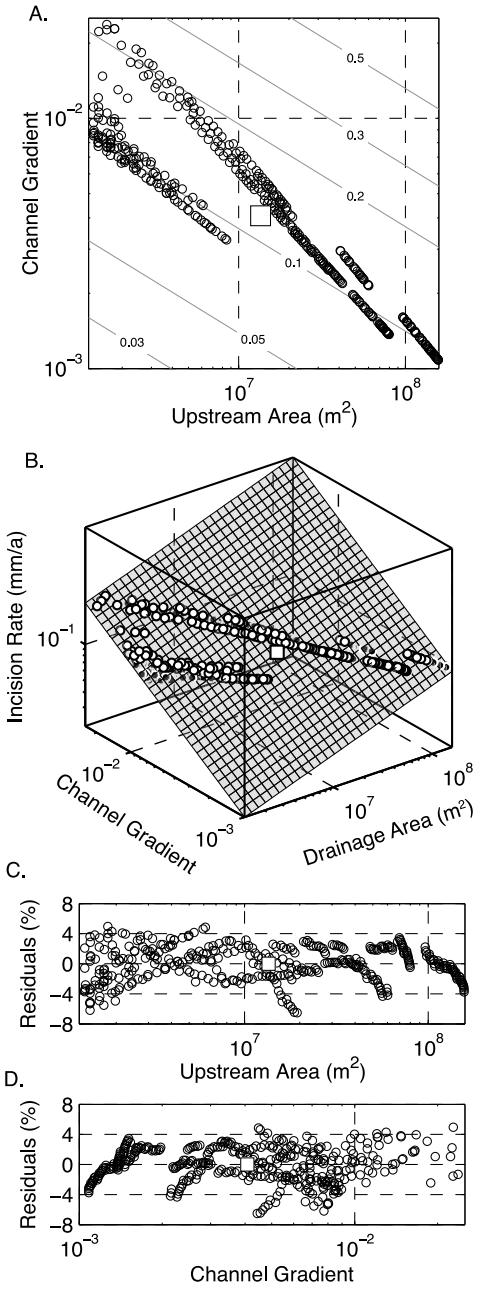

Figure 6. The same plots as shown in Figure 4, but with data from experiment using the nonlinear uplift pattern (sa_pup_3).

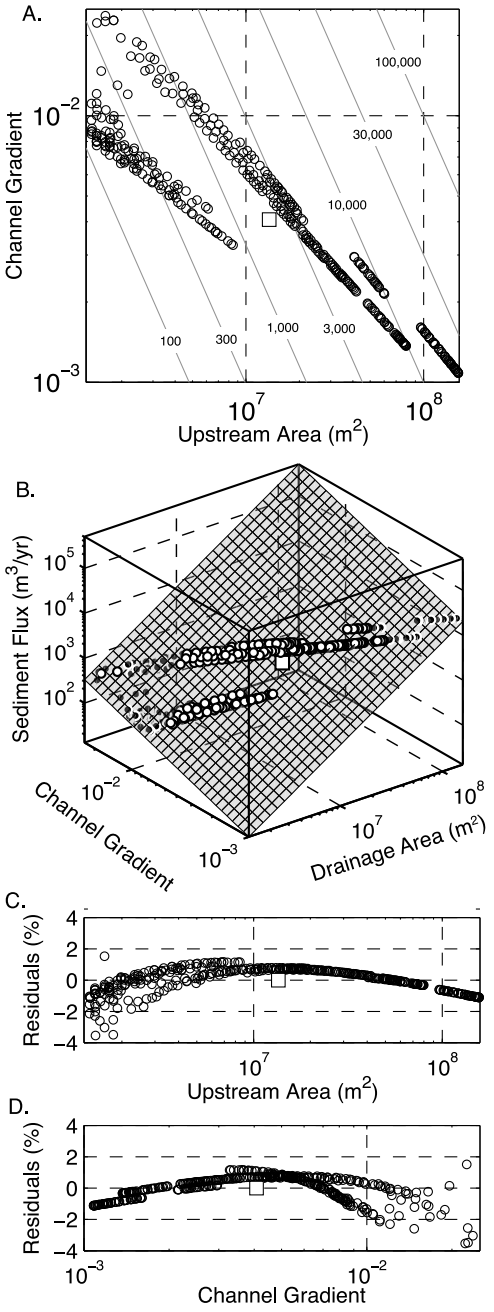

Figure 7. The same plots as shown in Figure 5, but with data from experiment using the nonlinear uplift pattern (sa_pup_3).

follows a power law relationship. This is perhaps not surprising given that we know that the water flux (discharge) is also well approximated by a power law. The difference, however, is that water discharge is only a function of A, whereas sediment flux is a function of both A and S. Slope tends to vary smoothly across a drainage network so that the value of S at a point is strongly correlated with the values of S in the network above that point.

[43] Table 3 and Figure 8 provide a comparison between the m' and n' values predicted from the incision models, and those estimated by the power law fit to the data. The observations and predictions have some noticeable differences but also show similar patterns. Comparing among the incision models, the observed m' and n' values are similar as long as the uplift patterns are the same. The predicted m' and n' values have greater differences among the models, especially when considering the transport-limited model, in which the predicted m' and n' values are constant.

[44] All of the observed m' and n' values fall along a linear trend with a slope of $\Delta m'/\Delta n' \approx 0.4$ and an intercept close to the origin (Figure 8). The nonlinear uplift cases always plot on the low side of this trend, and the linear uplift cases, on the high side. The predicted m' and n' values for numerical experiments using the saltation-abrasion and generalized abrasion models also show linear trends. These trends are offset upward from the trends for the observed values, indicating that the predicted m' values are slightly larger than the observed. The slopes of these trend lines are otherwise similar to those for the observed values. The prediction for the numerical experiments using the transport-limited incision model is that m' and n' should be constant at 0.32 and 1, respectively. The prediction fails to account for the trend in the observed data. We suspect that this problem

Table 3. Observed and Predicted Parameters for Power Law Approximation[a]

	Observed				Predicted	
Experiment	K'	m'	n'	R^2_{fit}	$\langle m' \rangle$	$\langle n' \rangle$
Saltation-Abrasion, Nonlinear						
sa_pup_1	1.20E-04	0.20	0.68	0.99	0.39	0.82
sa_pup_2	1.94E-04	0.20	0.68	0.99	0.35	0.68
sa_pup_3	4.88E-05	0.30	0.72	0.99	0.26	0.47
Generalized Abrasion, Nonlinear						
ga_pup_1	6.24E-05	0.26	0.74	0.94	0.29	0.60
ga_pup_2	1.05E-04	0.25	0.72	0.95	0.21	0.50
ga_pup_3	1.79E-05	0.36	0.76	0.94	0.32	0.59
Transport-Limited, Nonlinear						
tl_pup_1	1.51E-04	0.18	0.69	0.96	0.32	1.00
Stream Power, Nonlinear						
sp_pup_1	1.00E-05	0.50	1.00	1.00	0.50	1.00
sp_pup_2	1.00E-05	0.50	1.00	1.00	0.50	1.00
sp_pup_3	3.00E-06	0.50	1.00	1.00	0.50	1.00
sp_pup_4	5.00E-06	0.50	1.00	1.00	0.50	1.00
sp_pup_5	5.00E-06	0.50	1.00	1.00	0.50	1.00
Saltation-Abrasion, Linear						
sa_lup_1	2.56E-05	0.42	1.20	0.87	0.55	1.21
sa_lup_2	3.80E-05	0.44	1.35	0.79	0.54	1.32
sa_lup_3	5.93E-05	0.42	1.22	0.87	0.54	1.16
Generalized Abrasion, Linear						
ga_lup_1	1.19E-05	0.47	1.20	0.82	0.56	1.15
ga_lup_2	2.51E-05	0.46	1.32	0.76	0.64	1.37
ga_lup_3	1.95E-05	0.48	1.21	0.82	0.59	1.19
Transport-Limited, Linear						
tl_lup_1	3.33E-05	0.42	1.19	0.88	0.32	1.00
tl_lup_2	2.93E-05	0.40	1.23	0.85	0.32	1.00
Stream Power, Linear						
sp_lup_1	1.00E-05	0.50	1.00	1.00	0.50	1.00
sp_lup_2	1.00E-05	0.50	1.00	1.00	0.50	1.00
sp_lup_3	5.00E-06	0.50	1.00	1.00	0.50	1.00
sp_lup_4	3.00E-06	0.50	1.00	1.00	0.50	1.00

[a]Units consistent with area in square meters, dimensionless slope, and incision rates in meters per year.

Table 4. Observed Values for Power Law Approximation for Sediment Flux

Experiment	K'_s [a]	m'_s	n'_s	R^2_{fit}	$\mathcal{R}_0$ [b]	$\mathcal{R}_{max}$–$\mathcal{R}_{min}$	$(1-2\mathcal{R}_0)/(1-\mathcal{R}_0)$
Saltation-Abrasion, Nonlinear							
sa_pup_1	3.41E-06	1.52	0.98	1.00	0.96	1.0–0.83	−20.8
sa_pup_2	6.64E-06	1.52	0.99	1.00	0.95	1.0–0.82	−20.2
sa_pup_3	7.57E-06	1.52	1.00	1.00	0.97	1.0–0.91	−31.3
Generalized Abrasion, Nonlinear							
ga_pup_1	7.37E-07	1.64	1.08	1.00	0.86	0.98–0.54	−5.3
ga_pup_2	1.50E-06	1.63	1.08	1.00	0.88	0.98–0.54	−6.1
ga_pup_3	1.40E-06	1.64	1.08	1.00	0.86	0.97–0.54	−5.0
Transport-Limited, Nonlinear							
tl_pup_1	3.40E-06	1.51	1.00	1.00	0.99	1.0–0.94	–
Saltation-Abrasion, Linear							
sa_lup_1	3.17E-06	1.51	0.95	1.00	0.94	1.0–0.77	−14.4
sa_lup_2	4.89E-06	1.49	0.73	0.99	0.89	1.0–0.43	−7.1
sa_lup_3	6.09E-06	1.51	0.95	1.00	0.94	1.0–0.76	−14.0
Generalized Abrasion, Linear							
ga_lup_1	1.14E-06	1.58	0.97	1.00	0.86	0.99–0.54	−5.3
ga_lup_2	2.81E-06	1.56	0.94	1.00	0.88	1.0–0.55	−6.1
ga_lup_3	2.04E-06	1.58	0.96	1.00	0.86	0.99–0.54	−5.2
Transport-Limited, Linear							
tl_lup_1	5.02E-06	1.51	1.00	1.00	0.99	1.0–0.93	–
tl_lup_2	3.40E-06	1.51	0.99	1.00	0.99	1.0–0.93	–

[a]Constant assumes area is in square meters, slope is dimensionless, and sediment flux is in cubic meters per year.
[b]Log mean of observed $\mathcal{R}$ values in experiment.

is related to our assumption that the concavity of the river channels is relatively uniform over the numerical experiment (see discussion above in association with equation (24)).

[45] The trends in m'–n' space for numerical experiments using the abrasion models have different controlling factors. The m'–n' trend for the saltation-abrasion model is controlled by variation in bed cover, as represented by $\mathcal{R}$. The equation for the prediction of exponents when using the abrasion models ((21a) and (21b)) is very sensitive to changes in $\mathcal{R}$, as represented by the quantity $\frac{1-2\mathcal{R}_0}{1-\mathcal{R}_0}$ on the right side of (21a) and (21b). Table 4 shows that small changes in $\mathcal{R}_0$ result in large changes in $\frac{1-2\mathcal{R}_0}{1-\mathcal{R}_0}$. The focused erosion pattern in the numerical experiments with nonlinear uplift result in more negative values for $\frac{1-2\mathcal{R}_0}{1-\mathcal{R}_0}$. This quantity is present in the predictions for both m' and n', so more focused erosion tends to drive both exponents to smaller values.

[46] Those numerical experiments using the generalized abrasion model have a narrower range of $\mathcal{R}_0$ values. The values for $\frac{1-2\mathcal{R}_0}{1-\mathcal{R}_0}$ also have a narrow range. For these numerical experiments, the variation in m' and n' appears to be controlled by variation in the spatial pattern of sediment flux, which is expressed in the values of the exponents m'_s and n'_s (Table 4). The focused erosion pattern in the nonlinear uplift numerical experiments results in larger values for m'_s and n'_s, relative to those for the linear uplift experiments. These variations affect both m' and n', which explains why m' and n' tend to vary along a specific trend.

[47] The nonlinear form of $\mathcal{R}(1-\mathcal{R})$, which is present in both of the abrasion models ((14) and (15)), does not strongly influence our results. Figure 9 shows a plot of $\mathcal{R}(1-\mathcal{R})$ as a function of the flux-capacity ratio $\mathcal{R}$. The function $\mathcal{R}(1-\mathcal{R})$ has the form of an inverted parabola, with the tools dominating on the low side ($\mathcal{R} < 0.5$), and cover, on the high side ($\mathcal{R} > 0.5$). The power law approximation for $\mathcal{R}(1-\mathcal{R})$ only applies when the fluvial system is located entirely on one side or the other of this parabola. This is illustrated by the log-log plot (Figure 9b). The flanks of the parabola have relatively constant slopes in log-log space. The top of the parabola does not. Our experimental runs all lie on the high side, or "cover side" of the parabola (see $\mathcal{R}_0$ and $\mathcal{R}_{max}$–$\mathcal{R}_{min}$ in Table 4), which means that the power law approximation is appropriate.

[48] We summarize the results of the numerical experiment with five general observations.

[49] (1) The predictions show that the power law approximation for incision rates (equation (1)) applies for all of the tested incision models.

[50] (2) The numerical experiments show that the power law approximation applies over a range of at least an order of magnitude or more in area and slope values.

[51] (3) The numerical experiments show that the power law approximation holds for different patterns of uplift.

[52] (4) The power law exponents m' and n' are strongly dependent on the distribution of erosion. The m'/n' ratio remains fairly constant for any specific incision model, but the values themselves tend to become smaller as erosion

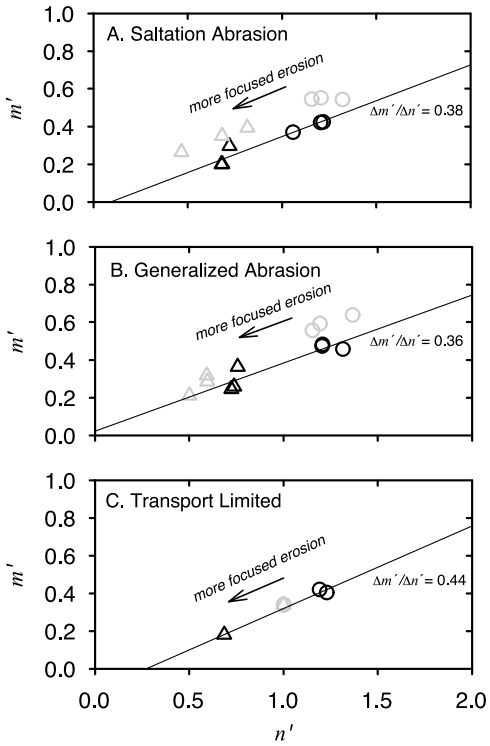

Figure 8. Comparison of observed (black symbols) and predicted (gray symbols) values for m' and n' for (a) saltation-abrasion, (b) generalized abrasion, and (c) transport-limited incision models. The circles are values from experiments with the linear uplift pattern; the triangles are values from experiments with the nonlinear uplift pattern. The black line marks the average trend for the observed m' and n' values.

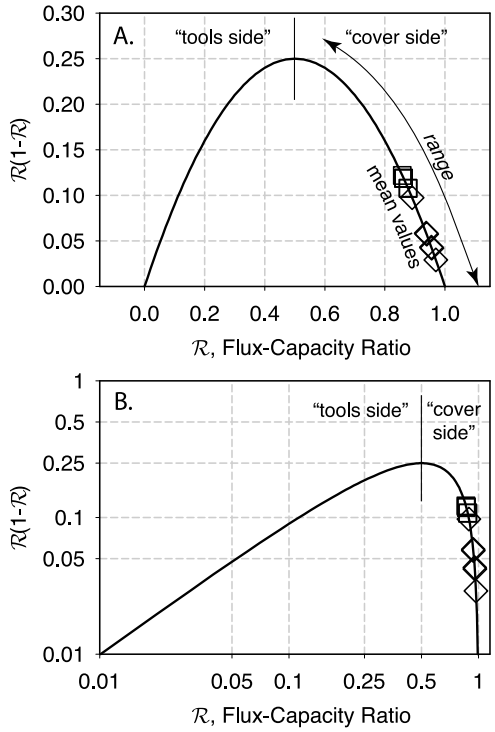

Figure 9. Plots showing $\mathcal{R}(1-\mathcal{R})$ as a function of $\mathcal{R}$. (a) The inverted parabolic form of this function. (b) The same with log-log axes. The diamonds and squares show $\mathcal{R}_0$ values for those experiments using the saltation-abrasion or general abrasion incision model, respectively. The range labeled in Figure 9a shows the range in $\mathcal{R}$ values within the model domain for these experiments.

becomes more focused within the highest part of the drainage.

[53] (5) The values of m' and n', by themselves, cannot be used to identify the processes controlling bedrock incision.

6. Discussion

[54] The stream power model provides a simple framework for understanding the evolution of bedrock channels in tectonically active landscapes. However, our understanding of bedrock incision has improved over the last decade, most notably due to the introduction of the saltation-abrasion model of *Sklar and Dietrich* [2004], which was one of the first incision models to explicitly address how sediment flux affects incision. In hindsight, the stream power model appears too simple for any real application, and we find it surprising that incision rates governed by the more complex sediment-flux-dependent incision models can be described as a power law function with the same form as the stream power model.

[55] In the numerical examples, the power law approximation applies because the influence of sediment flux on channel incision, as described by the function $\mathcal{R}(1-\mathcal{R})$, can be approximated with a power law function of drainage area and slope (Figure 9). A power law approximation of $\mathcal{R}(1-\mathcal{R})$ only holds when the results fall entirely on the "tools" or "cover" side of function. In our examples, all of the channels are cover dominated, and the expectation is that most river channels will tend to evolve toward the cover side of the parabola. The reason is that channels that lie on the tools side will generate more sediment and bedcover. As a result, "tools-side" channels are unstable, and will tend to migrate toward a "cover-side" condition. Channels with a "cover-side" condition will tend to be stable because of the negative feedback on this side of the parabola. Any increase in sediment (and bedcover) will result in a decrease in channel erosion. Laboratory experiments support this theory [*Johnson and Whipple*, 2007].

[56] Our examples illustrate how a power law approximation holds for channel incision when the influence of the sediment flux can also be approximated by a power law. However, we surmise that a power law relationship between channel incision, slope and drainage area will also apply when other variables beyond sediment flux influence incision rate. The key for the power law approximation is that the variables that influence bedrock incision must vary as a power law function of channel slope and (or) drainage area. An example of such a variable is channel width, which can often be described as a power law function of drainage area [e.g., *Montgomery and Gran*, 2001].

[57] An important distinction between the results presented in our study and the stream power model is that the power law parameters produced from the best fit to model data are not only a function of local incision processes, but also dependent on the distribution of bedrock uplift rates and sediment production within the drainage. This relationship indicates that there is a more complex interaction between tectonics and fluvial incision. In other words, one needs to consider not only the uplift rate at a point, but also the pattern of uplift rates across a drainage. Many analytical analyses of the interaction of tectonics and climate in convergent wedges have assumed that uplift rates are uniform across the landscape and that incision rates are governed by a stream power relationship with fixed values for m and n [*Roe et al.*, 2006; *Whipple and Meade*, 2004; *Whipple*, 2009]. However, our analysis suggests that if uplift rates are not uniform, the values of m and n may not be fixed among different landscapes.

[58] Existing geodynamic modeling provides some guidance about why uplift rates may vary across an orogenic wedge. For this purpose, we refer to the numerical model of *Fuller et al.* [2006], which explores the full evolution of a generic convergent wedge, where accretion, heat transport, rheology, and flexural isostasy are all accounted for in a geologically realistic manner. For our purposes here, the important conclusion of this work is that as a wedge grows, uplift rates tend to get localized into the central and highest part of the wedge. The reason is that as the wedge grows and thickens, the base of the wedge will become hot enough for viscous deformation to outpace frictional deformation. This thermally activated viscous softening starts when the maximum thickness of the wedge exceeds about 20 km. The central part of the wedge is now weaker and will tend to thicken faster than other parts of the wedge. Faster thickening will result in faster rock uplift at the surface of the wedge, which will lead to faster incision and erosion. Faster erosion will also cause isotherms to migrate upward beneath the center of the wedge, resulting in a larger viscous region at the base of the wedge. This localization of uplift and

erosion is similar to the tectonic aneurysm of *Koons et al.* [2002].

[59] A number of recent studies [*Hilley et al.*, 2004; *Roe et al.*, 2006, 2008; *Whipple and Meade*, 2004, 2006] indicate that m' is the essential variable for understanding the sensitivity of an orogenic wedge to changes in climate or tectonic forcing. We focus here on how the width, L, of a steady state orogenic wedge is influenced by tectonic forcing, as represented by the accretion rate, F, and climatic forcing, as represented by the precipitation rate, P. *Roe et al.* [2006] show that

$$\frac{\Delta L}{L} = \left(\frac{h}{m' + h}\right)\frac{\Delta F}{F} - \left(\frac{m'h}{m' + h}\right)\frac{\Delta P}{P}, \tag{27}$$

where h is Hack's constant [*Hack*, 1957]. (Note that *Roe et al.* [2006] use the reciprocal of this variable, but it is more typical to define h as used here.) Equation (27) shows how L will change given a change in F or P. As m' increases, the sensitivity of L to changes in P increases and to changes in F decreases. To say more, we need to know what the likely values of m' might be.

[60] In the past, m' was thought to fall somewhere in the range 1/3 to 1 [e.g., *Roe et al.*, 2006], but those estimates did not account for the role of sediment flux. Our work here shows that for abrasion-dependent incision, m' is a function of the distribution of sediment flux, which is controlled by the distribution of incision rates. Our numerical experiments indicate that under some conditions, m' values can be smaller. A low m' value means a weak sensitivity to climate change but a strong sensitivity to tectonic change. Consider our lowest value, $m' \approx 0.2$. A doubling of precipitation rate would cause the width of the orogen to decrease by only 15%. In contrast, a doubling of the accretion rate would cause orogen width to increase by 50%. As m' goes to zero, the climate sensitivity of the orogen goes to zero, and the tectonic sensitivity goes to one.

[61] A similar issue concerns the sensitivity of incision and erosion rates to changes in the character of fluvial discharge [e.g.; *Molnar*, 2001; *Snyder et al.*, 2003; *Tucker*, 2004]. In particular, *Molnar* [2001] has argued that Quaternary climate may be dominated by flashier discharges. He proposed this idea to explain the large increase, by a factor of 2 to 4, in the delivery of continent-derived sediments to the deep oceans over the last several million years. *Pelletier* [2009] has argued that Quaternary incision is faster in the Rockies due to an increased snowpack which leads to flashier discharges when the snowpack melts. These arguments imply incision rates are highly sensitive to discharge. Our results suggest that if m' is small, these conclusions may not apply.

[62] We consider an artificial example, where during a warm climate regime, the runoff moves off the landscape at a steady rate. A change to a colder climate regime would cause winter precipitation to be stored as snow. To a first approximation, we might expect the discharge to increase by a factor of two, since the annual precipitation is now moving through the drainage in half the time. If $m' \approx 0.2$, then this doubling in discharge would result in a 15% increase in incision rates. If flashier discharges were the cause of the increased sedimentation rates by a factor of 2 or more in the deep oceans [*Molnar*, 2001], then effective discharge would have to increase by a factor of 32. Our analysis here is simplified, mainly because the incision models we have examined provide only a limited approximation for the effect of a threshold shear stress (see discussion associated with equations (6) and (7)). Our intention is not to make specific predictions but rather to show the important influence that sediment flux may have in suppressing the incision process in bedrock rivers.

[63] We are left with an important question: Is there a lower limit for m'? The prediction equation (21a) allows both positive and negative values. We contend that the practical lower limit for m' is zero. If m' were less then zero, the result would look nothing like a fluvial landscape. The reason is that the channel localization process would be inverted. Areas where overland flow converged would erode more slowly than areas where flow diverged. In other words, "incision" would be fastest on interfluves and slowest in valleys. The resulting landscape would be smooth, rather than channelized. The expectation is that m' is always greater than zero in natural settings.

[64] There are few examples where m' and n' have been measured in real fluvial landscapes. *Stock and Montgomery* [1999] analyzed rivers from Hawaii, Australia, California, and Japan where long-term incision rates could be estimated. They inverted for K', m' and n' using a power law formulation. Seven of the rivers had low m' values (0.1 to 0.2), three had values 0.3 to 0.5, and one >2. *van der Beek and Bishop* [2003] reanalyzed some of the Australian rivers and found similar m' values. These m' values estimated from real landscapes are in the same range as those estimated from our numerical experiments.

[65] There is much debate at present about the influence of Late Cenozoic climate change on mountainous topography [e.g., *Molnar*, 2004; *Zhang et al.*, 2001]. Increases in alpine glaciation may play an important role in this debate, but our results suggest that some uplift patterns may lead to fluvial incision rates that are relatively insensitive to changes in discharge. This result may account for the prolonged steadiness of topography in the Olympic Mountains, which has remained close to a flux steady state since about 15 Ma [*Batt et al.*, 2001; *Brandon et al.*, 1998; *Pazzaglia and Brandon*, 2001]. Rock uplift and erosion are focused in the core of that range, so low m' values would be expected and have been demonstrated locally for the Clearwater drainage [*Tomkin et al.*, 2003].

[66] A number of recent studies have debated the possibility of large changes in the size of the Alps, starting at about 6 Ma [*Cederbom et al.*, 2004; *Champagnac et al.*, 2009; *Kuhlemann*, 2000; *Willett et al.*, 2006]. *Kuhlemann* [2000] showed that the sediment flux from the Alps increased several fold at about 5 Ma, but it is not known if that increase was due primarily to faster erosion of bedrock in the mountainous parts of the Alps or to removal of foreland basin sediments. Others have made arguments based on a change to a wetter climate over the Alps in the last 6 Ma [*Willett et al.*, 2006]. In contrast, *Bernet et al.* [2001, 2009] have reported an extensive suite of detrital cooling ages derived from the basement core of the Alps and deposited over the last 30 Ma in sedimentary basins surrounding the Alps. These data indicate that erosion rates in the core of the Alps have been steady over the last 30 Ma. While we do not intend to resolve this debate, we point out

that in the Alps uplift and erosion are focused in the highest part of the drainage [*Bernet et al.*, 2001, 2009; *Champagnac et al.*, 2009; *Wittmann et al.*, 2007]. Our results suggest that this situation may lead to fluvial incision rates in the Alps that are largely insensitive to changes in discharges.

7. Conclusions

[67] Our study suggests that a power law scaling relationship between incision rate, drainage area, and channel gradient likely applies in many settings, but the values of the scaling exponents vary depending on the pattern of rock uplift rates and the distribution of sediment flux across a drainage network. In mountain belts where high uplift rates are concentrated at the core of the range, the drainage area exponent is suppressed. Although we only explore incision models that include channel gradient, sediment flux, and drainage area, we surmise that a power law relationship will also exist even where other variables influence incision rate, so long as they vary smoothly and monotonically across a drainage network. This may explain why the stream power model, which seems incomplete, appears to explain the relationship between area, gradient and incision rate.

[68] Because scaling exponents in the incision relationship are likely not uniform among mountain ranges, incision rates in different settings will have different sensitivities to changes in discharge and climate. Furthermore, because the scaling exponent between incision rate and drainage area controls the sensitivity of orogen width to changes in both incoming accretionary flux and precipitation rate, regional uplift patterns play a first order role in controlling the size of mountain belts.

Notation

ι, α, σ natural log of incision rate, drainage area, and change gradient.

ι_0, α_0, σ_0 center point for power law approximation in ι–α–σ space.

ι_i^{obs}, ι_i^{pred} observation and prediction for incision rate at ith point in ι–α–σ space.

τ_b, τ_c basal and critical shear stress, [M L^{-1} T^{-2}].

b area exponent in width-discharge equation.

c area exponent in area-discharge equation.

$f(Q_s)$ sediment-flux erodibility function, [L^2 T^{-1}].

h Hack's exponent.

m', $\langle m' \rangle$ observed and predicted area exponent for power law approximation.

m'_s empirical area exponent for power law approximation for sediment flux.

m_i area exponent for detachment-limited equations.

m_t area exponent for sediment-transport equation.

n', $\langle n' \rangle$ observed and predicted slope exponent for power law approximation.

n'_s observed area exponent for power law approximation for sediment flux.

n_i slope exponent for detachment-limited equations.

n_t slope exponent for sediment-transport equation.

p_1 shear-stress exponent for detachment-limited equations.

p_2 water-discharge exponent for basal shear-stress equation.

p_3 slope exponent for basal shear-stress equation.

p_4 exponent for transport-capacity equation.

s downstream channel length, [L].

A drainage area, [L^2].

A_0 area at center point for power law approximation, [L^2].

F accretion rate, [L^2 T^{-1}].

I incision rate, [L T^{-1}].

I_0 incision rate at center point for power law approximation, [L T^{-1}].

K' constant in power law approximation for incision rate, [L$^{1-2m'}$T^{-1}].

K'_s constant in power law approximation for sediment flux, [L$^{3-2m'_s}$T^{-1}].

K_{GA} constant in generalized abrasion model, [L^{-1}].

K_{SA} constant in saltation-abrasion model, [L$^{-0.5}$].

K_{SP} constant in stream power model, [L^{1-2m}T^{-1}].

K_h constant in Hack's law, [L$^{1-2\ h}$].

K_t constant in sediment-transport equation, [L$^{3-2m_t}$T^{-1}].

L width of an orogenic wedge, [L].

P precipitation rate, [L T^{-1}].

Q_s sediment flux, [L^3 T^{-1}].

Q_t sediment-transport capacity, [L^3 T^{-1}].

Q_w water discharge, [L^3 T^{-1}].

$\mathcal{R}$ flux-capacity ratio.

R_0 flux-capacity ratio rate at center point for power law approximation.

R^2_{fit} quality index for best fit solution for power law approximation to data.

S channel gradient or slope.

S_0 channel gradient at center point for power law approximation.

U uplift rate, [L T^{-1}].

W channel width, [L].

Y_{divide} distance from open boundary to opposite closed boundary, [L].

M mass.

L length.

T time.

[69] **Acknowledgments.** This work was made possible by a Bateman Postdoctoral Fellowship at Yale University to Gasparini. Brandon was supported by the RETREAT project funded by the NSF Continental Dynamics Program (0208652). This project was designed by both Gasparini and Brandon. Gasparini conducted the experiments, and Brandon worked out the power law approximations. Gasparini and Brandon worked together with the interpretation and writing, with Gasparini in the lead. We are grateful for many useful discussions with Gerard Roe and Kelin Whipple. We also acknowledge helpful suggestions from the Associate Editor, George Hilley, and two anonymous reviewers.

References

Anders, A. M., et al. (2008), Influence of precipitation phase on the form of mountain ranges, *Geology*, *36*(6), 479–482, doi:10.1130/G24821A.1.

Batt, G. E., M. T. Brandon, K. A. Farley, and M. Roden-Tice (2001), Tectonic synthesis of the Olympic Mountains segment of the Cascadia wedge, using two-dimensional thermal and kinematic modeling of thermochronological ages, *J. Geophys. Res.*, *106*, 26,731–26,746, doi:10.1029/2001JB000288.

Belsley, D. A. (1991), *Conditioning Diagnostics: Collinearity and Weak Data in Regression*, John Wiley, New York.

Belsley, D. A., et al. (1980), *Regression Diagnostics: Identifying Influential Data and Sources of Collinearity*, Wiley-Interscience, Hoboken, N. J.

Bernet, M., et al. (2001), Steady-stale exhumation of the European Alps, *Geology*, *29*(1), 35–38, doi:10.1130/0091-7613(2001)029<0035:SSEOTE>2.0.CO;2.

Bernet, M., et al. (2009), Exhuming the Alps through time: Clues from detrital zircon fission-track thermochronology, *Basin Res.*, *21*(6), 781–798, doi:10.1111/j.1365-2117.2009.00400.x.

Brandon, M. T., et al. (1998), Late Cenozoic exhumation of the Cascadia accretionary wedge in the Olympic Mountains, northwest Washington State, *Geol. Soc. Am. Bull.*, *110*(8), 985–1009, doi:10.1130/0016-7606(1998)110<0985:LCEOTC>2.3.CO;2.

Cederbom, C. E., et al. (2004), Climate-induced rebound and exhumation of the European Alps, *Geology*, *32*(8), 709–712, doi:10.1130/G20491.1.

Champagnac, J. D., et al. (2009), Erosion-driven uplift of the modern Central Alps, *Tectonophysics*, *474*(1–2), 236–249, doi:10.1016/j.tecto.2009.02.024.

Chatanantavet, P., and G. Parker (2008), Experimental study of bedrock channel alluviation under varied sediment supply and hydraulic conditions, *Water Resour. Res.*, *44*, W12446, doi:10.1029/2007WR006581.

Chatanantavet, P., and G. Parker (2009), Physically based modeling of bedrock incision by abrasion, plucking, and macroabrasion, *J. Geophys. Res.*, *114*, F04018, doi:10.1029/2008JF001044.

Cowie, P. A., et al. (2008), New constraints on sediment-flux-dependent river incision: Implications for extracting tectonic signals from river profiles, *Geology*, *36*(7), 535–538, doi:10.1130/G24681A.1.

Crosby, B. T., K. X. Whipple, N. M. Gasparini, and C. W. Wobus (2007), Formation of fluvial hanging valleys: Theory and simulation, *J. Geophys. Res.*, *112*, F03S10, doi:10.1029/2006JF000566.

Dietrich, W. E., D. G. Bellugi, L. S. Sklar, J. D. Stock, A. M. Heimsath, and J. J. Roering (2003), Geomorphic transport laws for predicting landscape form and dynamics, in *Prediction in Geomorphology*, *Geophys. Monogr. Ser.*, vol. 135, edited by P. Wilcock and R. Iverson, pp. 103–132, AGU, Washington, D. C.

Duvall, A., E. Kirby, and D. Burbank (2004), Tectonic and lithologic controls on bedrock channel profiles and processes in coastal California, *J. Geophys. Res.*, *109*, F03002, doi:10.1029/2003JF000086.

Finnegan, N. J., et al. (2005), Controls on the channel width of rivers: Implications for modeling fluvial incision of bedrock, *Geology*, *33*(3), 229–232, doi:10.1130/G21171.1.

Finnegan, N. J., L. S. Sklar, and T. K. Fuller (2007), Interplay of sediment supply, river incision, and channel morphology revealed by the transient evolution of an experimental bedrock channel, *J. Geophys. Res.*, *112*, F03S11, doi:10.1029/2006JF000569.

Fuller, C. W., et al. (2006), Formation of forearc basins and their influence on subduction zone earthquakes, *Geology*, *34*(2), 65–68, doi:10.1130/G21828.1.

Gasparini, N. M., K. X. Whipple, and R. L. Bras (2007), Predictions of steady state and transient landscape morphology using sediment-flux-dependent river incision models, *J. Geophys. Res.*, *112*, F03S09, doi:10.1029/2006JF000567.

Hack, J. T. (1957), Studies of longitudinal stream profiles in Virginia and Maryland, *U.S. Geol. Surv. Prof. Pap., 294-B*, 43 pp.

Hassani, S. (2009), *Mathematical Methods for Students of Physics and Related Fields*, 2nd ed., 831 pp., Springer, New York.

Hilley, G. E., and M. R. Strecker (2004), Steady state erosion of critical Coulomb wedges with applications to Taiwan and the Himalaya, *J. Geophys. Res.*, *109*, B01411, doi:10.1029/2002JB002284.

Hilley, G. E., M. R. Strecker, and V. A. Ramos (2004), Growth and erosion of fold-and-thrust belts with an application to the Aconcagua fold-and-thrust belt, Argentina, *J. Geophys. Res.*, *109*, B01410, doi:10.1029/2002JB002282.

Howard, A. D. (1980), Thresholds in river regimes, in *Thresholds in Geomorphology*, edited by D. R. Coates and J. D. Vitek, pp. 227–258, Allen and Unwin, London.

Howard, A. D. (1994), A detachment-limited model of drainage basin evolution, *Water Resour. Res.*, *30*, 2261–2285, doi:10.1029/94WR00757.

Howard, A. D., and G. Kerby (1983), Channel changes in badlands, *Geol. Soc. Am. Bull.*, *94*(6), 739–752, doi:10.1130/0016-7606(1983)94<739:CCIB>2.0.CO;2.

Howard, A. D., W. E. Dietrich, and M. A. Seidl (1994), Modeling fluvial erosion on regional to continental scales, *J. Geophys. Res.*, *99*(B7), 13,971–13,986, doi:10.1029/94JB00744.

Johnson, J. P., and K. X. Whipple (2007), Feedbacks between erosion and sediment transport in experimental bedrock channels, *Earth Surf. Processes Landforms*, *32*(7), 1048–1062, doi:10.1002/esp.1471.

Johnson, J. P. L., K. X. Whipple, L. S. Sklar, and T. C. Hanks (2009), Transport slopes, sediment cover, and bedrock channel incision in the Henry Mountains, Utah, *J. Geophys. Res.*, *114*, F02014, doi:10.1029/2007JF000862.

Kirby, E., and K. Whipple (2001), Quantifying differential rock-uplift rates via stream profile analysis, *Geology*, *29*(5), 415–418, doi:10.1130/0091-7613(2001)029<0415:QDRURV>2.0.CO;2.

Koons, P. O., et al. (2002), Mechanical links between erosion and metamorphism in Nanga Parbat, Pakistan Himalaya, *Am. J. Sci.*, *302*(9), 749–773, doi:10.2475/ajs.302.9.749.

Kuhlemann, J. (2000), Post-collisional sediment budget of circum-Alpine basins (central Europe), *Mem. Sci. Geol. Padova*, *52*, 1–91.

Leopold, L. B., et al. (1964), *Fluvial Processes in Geomorphology*, 522 pp., W. H. Freeman, London.

Meakin, P. (1998), *Fractals, Scaling, and Growth Far from Equilibrium*, 674 pp., Cambridge Univ. Press, Cambridge.

Meyer-Peter, R., and R. Müller (1948), Formulas for bedload transport, in *Proceedings of the 2nd Meeting International Association of Hydraulic Research*, pp. 39–64, Int. Assoc. of Hydraul. Res., Delft, Netherlands.

Miller, S. R., and R. L. Slingerland (2006), Topographic advection on fault-bend folds: Inheritance of valley positions and the formation of wind gaps, *Geology*, *34*(9), 769–772, doi:10.1130/G22658.1.

Molnar, P. (2001), Climate change, flooding in arid environments, and erosion rates, *Geology*, *29*(12), 1071–1074, doi:10.1130/0091-7613(2001)029<1071:CCFIAE>2.0.CO;2.

Molnar, P. (2004), Late cenozoic increase in accumulation rates of terrestrial sediment: How might climate change have affected erosion rates?, *Annu. Rev. Earth Planet. Sci.*, *32*, 67–89, doi:10.1146/annurev.earth.32.091003.143456.

Montgomery, D. R., and K. B. Gran (2001), Downstream variations in the width of bedrock channels, *Water Resour. Res.*, *37*(6), 1841–1846, doi:10.1029/2000WR900393.

Ouimet, W. B., et al. (2009), Beyond threshold hillslopes: Channel adjustment to base-level fall in tectonically active mountain ranges, *Geology*, *37*(7), 579–582, doi:10.1130/G30013A.1.

Parker, G. (2004), Somewhat less random notes on bedrock incision, *Intern. Memo. 118*, 20 pp., St. Anthony Falls Lab., Univ. of Minn., Minneapolis.

Pazzaglia, F. J., and M. T. Brandon (2001), A fluvial record of long-term steady-state uplift and erosion across the Cascadia forearc high, western Washington State, *Am. J. Sci.*, *301*(4–5), 385–431, doi:10.2475/ajs.301.4-5.385.

Pelletier, J. D. (2009), The impact of snowmelt on the late Cenozoic landscape of the southern Rocky Mountains, USA, *GSA Today*, *19*(7), 4–11, doi:10.1130/GSATG44A.1.

Pelletier, J. D. (2010), Numerical modeling of the late Cenozoic geomorphic evolution of Grand Canyon, Arizona, *Geol. Soc. Am. Bull.*, *122*(3–4), 595–608, doi:10.1130/B26403.1.

Roe, G. H., et al. (2002), Effects of orographic precipitation variations on the concavity of steady-state river profiles, *Geology*, *30*(2), 143–146, doi:10.1130/0091-7613(2002)030<0143:EOOPVO>2.0.CO;2.

Roe, G. H., D. R. Montgomery, and B. Hallet (2003), Orographic precipitation and the relief of mountain ranges, *J. Geophys. Res.*, *108*(B6), 2315, doi:10.1029/2001JB001521.

Roe, G. H., et al. (2006), Response of a steady-state critical wedge orogen to changes in climate and tectonic forcing, in *Tectonics, Climate, and Landscape Evolution*, edited by S. D. Willett et al., *Spec. Pap. Geol. Soc. Am.*, *398*, 227–239, doi:10.1130/2005.2398(13).

Roe, G. H., et al. (2008), Feedbacks among climate, erosion, and tectonics in a critical wedge orogen, *Am. J. Sci.*, *308*, 815–842, doi:10.2475/07.2008.01.

Rosenbloom, N. A., and R. S. Anderson (1994), Hillslope and channel evolution in a marine terraced landscape, Santa Cruz, California, *J. Geophys. Res.*, *99*(B7), 14,013–14,029, doi:10.1029/94JB00048.

Savageau, M. A. (1988), Introduction to S-systems and the underlying power-law formalism, *Math. Comput. Model.*, *11*, 546–551, doi:10.1016/0895-7177(88)90553-5.

Savageau, M. A., and E. O. Voit (1987), Recasting nonlinear differential equations as S-systems: A canonical nonlinear form, *Math. Biosci.*, *87*(1), 83–115, doi:10.1016/0025-5564(87)90035-6.

Seidl, M. A., and W. E. Dietrich (1992), The problem of channel erosion into bedrock, *Catena Suppl.*, *23*, 101–124.

Sinha, S. K., and G. Parker (1996), Causes of concavity in longitudinal profiles of rivers, *Water Resour. Res.*, *32*, 1417–1428, doi:10.1029/95WR03819.

Sklar, L. S., and W. E. Dietrich (2001), Sediment and rock strength controls on river incision into bedrock, *Geology*, *29*(12), 1087–1090, doi:10.1130/0091-7613(2001)029<1087:SARSCO>2.0.CO;2.

Sklar, L. S., and W. E. Dietrich (2004), A mechanistic model for river incision into bedrock by saltating bed load, *Water Resour. Res.*, *40*, W06301, doi:10.1029/2003WR002496.

Sklar, L. S., and W. E. Dietrich (2006), The role of sediment in controlling steady-state bedrock channel slope: Implications of the saltation-abrasion incision model, *Geomorphology*, *82*(1–2), 58–83, doi:10.1016/j.geomorph.2005.08.019.

Snyder, N. P., et al. (2000), Landscape response to tectonic forcing: Digital elevation model analysis of stream profiles in the Mendocino triple junc-

tion region, northern California, *Geol. Soc. Am. Bull.*, *112*(8), 1250–1263, doi:10.1130/0016-7606(2000)112<1250:LRTTFD>2.0.CO;2.

Snyder, N. P., K. X. Whipple, G. E. Tucker, and D. J. Merritts (2003), Correction to "Importance of a stochastic distribution of floods and erosion thresholds in the bedrock river incision problem," *J. Geophys. Res.*, *108* (B8), 2388, doi:10.1029/2003JB002649.

Stock, J. D., and D. R. Montgomery (1999), Geologic constraints on bedrock river incision using the stream power law, *J. Geophys. Res.*, *104*, 4983–4993, doi:10.1029/98JB02139.

Stolar, D. B., et al. (2006), Climatic and tectonic forcing of a critical orogen: Findings from a numerical sandbox, in *Tectonics, Climate, and Landscape Evolution*, edited by S. D. Willett et al., *Spec. Pap. Geol. Soc. Am.*, *398*, 241–250, doi:10.1130/2006.2398(14).

Tomkin, J. H., M. T. Brandon, F. J. Pazzaglia, J. R. Barbour, and S. D. Willett (2003), Quantitative testing of bedrock incision models for the Clearwater River, NW Washington State, *J. Geophys. Res.*, *108*(B6), 2308, doi:10.1029/2001JB000862.

Tucker, G. E. (2004), Drainage basin sensitivity to tectonic and climatic forcing: Implications of a stochastic model for the role of entrainment and erosion thresholds, *Earth Surf. Processes Landforms*, *29*, 185–205, doi:10.1002/esp.1020.

Tucker, G. E., and R. L. Bras (1998), Hillslope processes, drainage density, and landscape morphology, *Water Resour. Res.*, *34*, 2751–2764, doi:10.1029/98WR01474.

Tucker, G. E., and R. Slingerland (1996), Predicting sediment flux from fold and thrust belts, *Basin Res.*, *8*(3), 329–349, doi:10.1046/j.1365-2117.1996.00238.x.

Tucker, G. E., and K. X. Whipple (2002), Topographic outcomes predicted by stream erosion models: Sensitivity analysis and intermodel comparison, *J. Geophys. Res.*, *107*(B9), 2179, doi:10.1029/2001JB000162.

Tucker, G., et al. (2001a), The Channel-Hillslope Integrated Landscape Development Model (CHILD), in *Landscape Erosion and Evolution Modeling*, edited by R. Harmon and W. Doe III, pp. 349–388, Kluwer Acad., New York.

Tucker, G. E., et al. (2001b), An object-oriented framework for distributed hydrologic and geomorphic modeling using triangulated irregular networks, *Comput. Geosci.*, *27*(8), 959–973, doi:10.1016/S0098-3004(00)00134-5.

Turowski, J. M., D. Lague, and N. Hovius (2007), Cover effect in bedrock abrasion: A new derivation and its implications for the modeling of bedrock channel morphology, *J. Geophys. Res.*, *112*, F04006, doi:10.1029/2006JF000697.

van der Beek, P., and P. Bishop (2003), Cenozoic river profile development in the Upper Lachlan catchment (SE Australia) as a test of quantitative fluvial incision models, *J. Geophys. Res.*, *108*(B6), 2309, doi:10.1029/2002JB002125.

Voit, E. O. (2000), *Computational Analysis of Biochemical Systems: A Practical Guide for Biochemists and Molecular Biologist*, Cambridge Univ. Press, New York.

Voit, E. O., and M. A. Savageau (1987), Accuracy of alternative representations for integrated biochemical systems, *Biochemistry*, *26*(21), 6869–6880, doi:10.1021/bi00395a042.

Whipple, K. X. (2009), The influence of climate on the tectonic evolution of mountain belts, *Nat. Geosci.*, *2*(2), 97–104, doi:10.1038/ngeo413.

Whipple, K. X., and B. J. Meade (2004), Controls on the strength of coupling among climate, erosion, and deformation in two-sided, frictional orogenic wedges at steady state, *J. Geophys. Res.*, *109*, F01011, doi:10.1029/2003JF000019.

Whipple, K. X., and B. J. Meade (2006), Orogen response to changes in climatic and tectonic forcing, *Earth Planet. Sci. Lett.*, *243*(1–2), 218–228, doi:10.1016/j.epsl.2005.12.022.

Whipple, K. X., and G. E. Tucker (1999), Dynamics of the stream-power river incision model: Implications for height limits of mountain ranges, landscape response timescales, and research needs, *J. Geophys. Res.*, *104*(B8), 17,661–17,674, doi:10.1029/1999JB900120.

Whipple, K. X., and G. E. Tucker (2002), Implications of sediment-flux-dependent river incision models for landscape evolution, *J. Geophys. Res.*, *107*(B2), 2039, doi:10.1029/2000JB000044.

Whittaker, A. C., et al. (2007), Bedrock channel adjustment to tectonic forcing: Implications for predicting river incision rates, *Geology*, *35*(2), 103–106, doi:10.1130/G23106A.1.

Willemin, J. H. (2000), Hack's law: Sinuosity, convexity, elongation, *Water Resour. Res.*, *36*(11), 3365–3374, doi:10.1029/2000WR900229.

Willett, S. D., et al. (2006), Messinian climate change and erosional destruction of the central European Alps, *Geology*, *34*(8), 613–616, doi:10.1130/G22280.1.

Willgoose, G., R. L. Bras, and I. Rodriguez-Iturbe (1991), A coupled channel network growth and hillslope evolution model: 1. Theory, *Water Resour. Res.*, *27*, 1671–1684, doi:10.1029/91WR00935.

Wittmann, H., F. von Blanckenburg, T. Kruesmann, K. P. Norton, and P. W. Kubik (2007), Relation between rock uplift and denudation from cosmogenic nuclides in river sediment in the Central Alps of Switzerland, *J. Geophys. Res.*, *112*, F04010, doi:10.1029/2006JF000729.

Wobus, C. W., et al. (2003), Has focused denudation sustained active thrusting at the Himalayan topographic front?, *Geology*, *31*(10), 861–864, doi:10.1130/G19730.1.

Wobus, C., et al. (2006), Tectonics from topography: Procedures, promise, and pitfalls, in *Tectonics, Climate, and Landscape Evolution*, edited by S. D. Willett et al., *Spec. Pap. Geol. Soc. Am.*, *398*, 55–74, doi:10.1130/2006.2398(04).

Wolman, M. G., and J. P. Miller (1960), Magnitude and frequency of forces in geomorphic processes, *J. Geol.*, *68*, 54–74, doi:10.1086/626637.

Yanites, B. J., et al. (2010), Incision and channel morphology across active structures along the Peikang River, central Taiwan: Implications for the importance of channel width, *Geol. Soc. Am. Bull.*, *122*(7–8), 1192–1208, doi:10.1130/B30035.1.

Zhang, P. Z., et al. (2001), Increased sedimentation rates and grain sizes 2–4 Myr ago due to the influence of climate change on erosion rates, *Nature*, *410*(6831), 891–897, doi:10.1038/35073504.

M. T. Brandon, Department of Geology and Geophysics, Yale University, PO Box 208109, 210 Whitney Ave., New Haven, CT 06520-8109, USA.

N. M. Gasparini, Department of Earth and Environmental Sciences, Tulane University, 101 Blessey Hall, New Orleans, LA 70118, USA. (ngaspari@tulane.edu)